Article:
Parker, J., Smith, R. and Cumming, D. (2024) High-resolution X-ray mapping of fluorinated binders in lithium-ion battery electrodes. The Journal of Physical Chemistry C, 128 (49). ISSN: 1932-7447

https://doi.org/10.1021/acs.jpcc.4c05678

THE JOURNAL OF PHYSICAL CHEMISTRY C
A JOURNAL OF THE AMERICAN CHEMICAL SOCIETY

pubs.acs.org/JPCC
Article

High-Resolution X-ray Mapping of Fluorinated Binders in Lithium-Ion Battery Electrodes

James Parker, Rachel Smith, and Denis Cumming*

Cite This: J. Phys. Chem. C 2024, 128, 20957−20966

ABSTRACT: This study looks at energy-dispersive X-ray spectroscopy (EDX) maps of fluorine in NMC 622 cathodes and the efforts made to improve the spatial resolution of fluorine mapping. The transition to electric vehicles demands faster and efficient production of next-generation lithium-ion batteries. To achieve this goal, the industry needs to take advantage of state-of-the-art battery characterization techniques in the pursuit of gaining a greater understanding of electrode structure and production. The binder location within an electrode is critical to electrochemical performance and contains fluorine, yielding an opportunity to use it as a marker and a way to visualize binder distribution and therefore, better understand process-structure relations. However, fluorine is difficult to differentiate from cobalt and manganese in an EDX spectrum due to similar Kα energy. Fluorine also interacts with the electron beam, potentially leading to poor spatial resolution. This paper examines different EDX parameters and compares the spatial resolution of fluorine in the maps of lithium-ion cathode cross sections. Analysis of the EDX maps showed that reducing the accelerating voltage from 20 to 5 kV improved the spatial resolution of fluorine 10-fold, from 2553 to 238 nm, supported by CASINO simulations. The EDX maps also indicated that imaging for one long scan at a 2500 μs dwell time produced a higher spatial resolution than imaging for 10 scans at 250 μs. Repeated line scans of the sample showed the extent of fluorine mobility; fluorine-rich zones emit less, while fluorine-free zones begin to emit more fluorine X-rays. This work shows that the spatial resolution of fluorine maps can be increased by imaging at 5 kV and scanning for one pass at 2500 μs. This methodology can be used to create more representative EDX maps of the binder in the cathodes. Visual analysis or further processing with an image analysis can reveal binder distributions and potential binder gradients. This technique is useful in understanding how changes to electrode manufacturing can change the electrode structure and binder distribution.

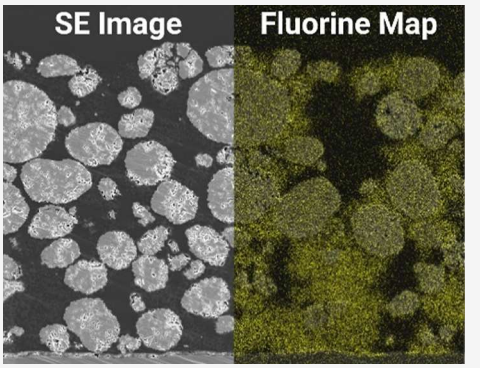

INTRODUCTION

Lithium-ion batteries are the leading technology in portable energy storage and are essential to powering a wide range of devices. Batteries store chemical potential energy, which can be converted to electrical energy on demand. This is accomplished by having two electrodes, an anode and a cathode. In a charged state, lithium ions and electrons are stored at the anode and can be discharged, transferring the ions and electrons to the cathode and producing a current. Batteries are designed to be efficient and possess a high energy capacity. The effectiveness of the electrodes within the battery greatly influences the capability of the battery.

As lithium-ion cell chemistries have advanced, industry and the literature have identified the manufacturing of electrodes to play a significant role in electrode performance.[1−3] Electrodes are formulated from three components: an active material, a conductive additive, and a binder. The role of the conductive additive and binder has been proven integral to electric conductivity and mechanical stability.[4−9] Together, the conductive additive and binder form a nanosized conductive binder domain (CBD).[10] Understanding the structure of the CBD is becoming increasingly paramount. This regime affects the surface coating and superficial pores of active particles and changes the pore network of the electrode.[11] Coating additions, interphase changes, and the alteration of pores significantly affect electrode impedance and stability.[12−15]

Poor manufacturing can often lead to electrode heterogeneity, a frequently encountered obstacle which causes reduced Coulombic efficiency and severe capacity degradation.[16] A notorious heterogeneity at the macroscale level is binder migration.[17] The binder migrates to the electrode surface, leaving a nonuniform distribution throughout the coating z-axis.[18] Binder migration occurs during rapid electrode drying.[17,19−21] Diagnosing the extent of the migration is critical in optimization and can be measured by imaging the electrode.

Received: August 22, 2024
Revised: October 28, 2024
Accepted: November 4, 2024
Published: December 2, 2024

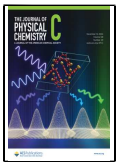

https://doi.org/10.1021/acs.jpcc.4c05678
J. Phys. Chem. C 2024, 128, 20957−20966

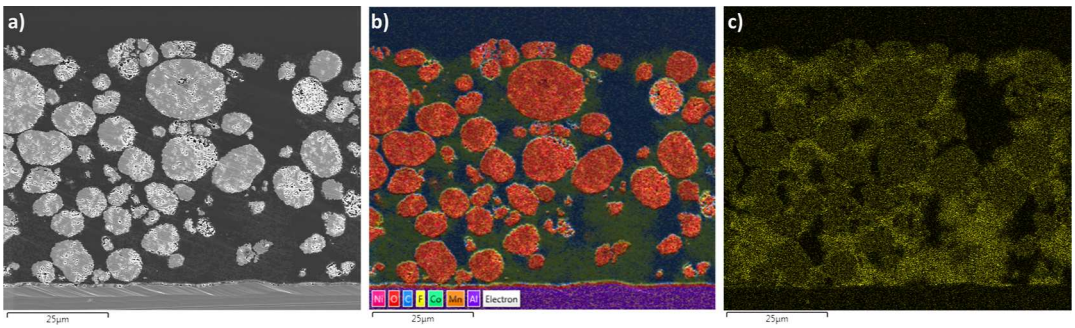

Figure 1. (a) Secondary electron image of a resin-impregnated electrode cross section, (b) equivalent layered EDX image, and (c) equivalent fluorine EDX map.

The particles involved in the carbon binder domain are nanosized[22] and require advanced techniques such as scanning electron microscopy (SEM) or X-ray computed tomography (XCT) to resolve. Both of these techniques have been previously utilized in the battery field. SEM of electrode cross sections has been conducted for both anodes[20] and cathodes.[23−25] XCT has been conducted from electrode to cell levels.[10] Studies have also combined XCT and EDX together in the pursuit of further CBD understanding.[11]

XCT can be a valuable technique due to being nondestructive and allowing whole-cell analysis; however, XCT imaging is performed by measuring X-ray attenuation which highly correlates with sample density.[26] This inhibits the differentiation of the conductive additive and binder because they are both carbon-dominated and together form the amorphous CBD structure. Limited photon flux, in conjunction with size and positioning restrictions of both the X-ray detector and the electrode sample, can prevent submicron spatial resolution in XCT[27] which is necessary to resolve the CBD phase.

SEM/EDX is an intrusive and destructive technique;[28−30] however, it can yield an abundance of information. Incidence electrons produced during SEM have nanometer wavelengths. This allows SEM to achieve exceptional spatial resolutions,[31] capable of resolving the CBD phase. A benefit of SEM is depicting the electrical conductivity within the image. Insufficiently conductive sections of the sample repel electrons and cause artifacts and charging; this can highlight poorly performing CBD.[32]

EDX also has the advantage of atomic identification and can simultaneously differentiate elements by their characteristic X-ray wavelengths.[33] PVDF is a dominant binder choice in slurry-cast cathodes due to its high voltage stability, mechanical properties, and thermal stability.[34−36] Fluorine is only present in the binder. Therefore, the mapping of fluorine allows for the mapping of the binder in cathodes. This technique could be used to identify binder gradients and binder agglomeration.[25] Studies have taken the EDX maps further by using image analysis software to quantify binder distributions along the *z*-axis for entire cross sections.[25]

Fluorine is a particularly problematic element to analyse due to being the most electronegative element and only emmitting relatively low-energy kα X-rays.[37] Additionally, cobalt and manganese have similar Kα X-ray energy and are in far greater concentration in an NMC cathode; therefore, their X-ray peaks can overlap significantly. This presents a challenge to accurately quantify each element. Industrial electrodes typically have greater than 90% active material[38] and only a few percent by weight of other additives, such as the fluorine-containing binder. The above complications cause fluorine X-rays to be a minimal fraction of the total X-ray emissions and require high-spectral-resolution EDX detectors to differentiate the fluorine signal from other elements. Additionally, consideration of the electron beam damaging the sample, causing phase transitions in NMC-811[39] and decay of fluorinated polymers into monomers,[40,41] is important. These challenges inspire the need for a robust microscopy procedure.

This paper aims to provide insight into the EDX fluorine within cathodes and efforts that can be made to develop the response and increase the spatial resolution. Two significantly important parameters for EDX are the dwell time and the accelerating voltage of the beam. SEM and EDX work by splitting the sample area into a grid and imaging each coordinate of the grid. Dwell time infers the amount of time each coordinate will be excited by the beam and measured by the X-ray detector. A higher dwell time will increase the total amount of X-rays emitted and measured. The other parameter, accelerating voltage, refers to the voltage induced to accelerate the electrons toward the sample. A higher voltage imparts more energy to each electron. This will cause the electrons to interact with a larger volume of the sample, known as the interaction volume.

EXPERIMENTAL SECTION

Slurry Mixing. The active material NMC 622 from BASF was mixed with Imery's C-NERGY Super C65 carbon black and Solvay's Solef 1015 PVDF, with an average molecular weight of 573 g mol^{-1}. Slurries were mixed in a solution of *N*-methyl-2-pyrrolidone (NMP) from Sigma-Aldrich (anhydrous, 99.5%). The final solid content was 60%, with a weight proportion of 92:4:4 of the active material, conductive additive, and binder.

All weighing steps were performed in an argon-controlled glovebox for an inert anhydrous atmosphere. Mixing was performed using a THINKY ARE-250 planetary mixer, and any mixing involving powder and liquids in one stage comprised adding the powder first and the liquid second. The mixing protocol involved dissolving PVDF to make an 8 wt % PVDF solution in NMP. This solution should be colorless if anhydrous. The carbon black was then added in addition to half the remaining NMP and mixed at 500 rpm for 1 min followed by mixing at 2000 rpm for 5 min. NMC was then added in addition to the other half of the remaining NMP and mixed at 500 rpm for 1 min followed by mixing at 2000 rpm for 15 min. The mixture was then degassed at 2200 rpm for 3 min.

https://doi.org/10.1021/acs.jpcc.4c05678
J. Phys. Chem. C 2024, 128, 20957−20966

Slurry Casting. The slurry was coated with a doctor blade at a rate of 1.3 m per minute and set at a height of 270 μm onto a 15 μm aluminum foil. The coating was dried in a fume cupboard on a heated drawdown coater set to 80 °C for 1 h before being transferred to an 80 °C vacuum oven to dry overnight. The initial coating of 55% porosity was then compressed to 45% using a heated double-roller calender set to a temperature of 60 °C.

Resin Casting. Samples were prepared by impregnating electrodes with epoxy resin, EpoFix resin from Agar Scientific, to make tombs. Before curing, the resin was vacuumed to 0.01 bar three times to remove gas bubbles. The resin compound consisted of organic compounds, C12−14 carbon chain polymers with alkoxy (−C−O−C−) and methyl ($-CH_3$) groups, limiting the resin's atomic makeup to carbon, hydrogen, and oxygen. These tombs were then ultramicrotomed for a diamond finish using a Leica ultramicrotome. 20 μm of the material was removed with 1 μm slices followed by an additional 20 μm of 0.5 μm slices using a glass knife. A diamond knife was then used to remove 70 nm slices until a minimum of 12 μm of the material was removed, and the offcuts were uniform in color and unfragmented. The samples were then ion-milled with a PECS II ion miller at 5 kV for 45 min, 2° incline, to remove any preparation damage to the active material particles. Samples were mounted on SEM stubs, earthed with silver paint, and carbon-coated to increase electrical conductivity. A resin-impregnated cathode cross section can be seen in Figure 1a.

Microscopy. EDX analysis was conducted using an FEI Inspect F50 scanning electron microscope with an Oxford Instruments X-Max 80 mm^2 silicon drift detector. The resolution of the EDX detector was 125 eV for the Mn K_α peak. EDX maps were run at 5 and 20 kV accelerating voltages. The dwell time for scans was also altered between 2500 and 250 μs. To control the imaging time, 10 scans were taken for 250 μs maps but only one scan for 2500 μs maps. Maps were conducted at a 3500× magnification. A layered EDX map of all detectable elements can be seen in Figure 1b. This map was taken at 2500 μs for one scan. The respective fluorine map for this scan is shown in Figure 1c. A longer process time of 5 was selected to help increase differentiation between fluorine, cobalt, and manganese. The average dead time was 35% when imaging the electrode. A spot size of 4 was used for SEM.

Line scans were conducted by selecting an appropriate site location where the CBD phase is visible at the electrode−resin interface, as demonstrated in Figure 2. Each line scan location was scanned a total of 5 times. A delay of 2 min was used between each scan, and beam blanking was enabled during this time to reduce current exposure. Line scans were conducted at a 300 or 1000 μs dwell time and at a 5 or 20 kV accelerating voltage.

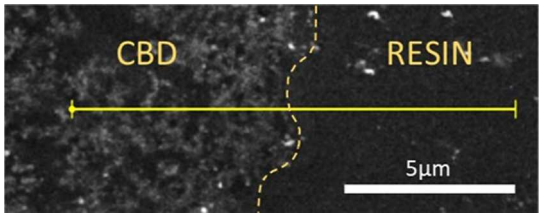

Figure 2. Secondary electron image showing the interface between the electrode CBD and CBD-free epoxy resin. The dashed yellow line marks the interface. The solid yellow line represents an exemplary line scan used to scan the interface between the CBD and epoxy resin that has been annotated.

CASINO Simulation. The electron trajectory and interactions were modeled and simulated in Monte Carlo Simulation software (CASINO) version 2.4.8. This software is specialized for Monte Carlo simulations of electron trajectories in solids. 1000 electrons were simulated interacting with the resin at 5 and 20 kV accelerating voltages. Epofix resin denotes the reactive polymer as bisphenol A-epichlorohydrin. The estimated stoichiometry for this polymer is shown in Table 1 with a density of 1.2 g cm^{-3}. The machine beam radius was estimated at 3 nm with a 0° specimen tilt.

Table 1. Stoichiometry for the Resin Used in CASINO Simulations

element	Z	atomic fraction
C	12	0.428
H	1	0.495
O	16	0.077

The stoichiometry for the epoxy resin was estimated and partitioned into carbon, hydrogen, and oxygen. This resin was used for all CASINO simulations (5 and 20 kV) to model the interaction volumes.

RESULTS AND DISCUSSION

Fluorine Maps of the PVDF Binder. EDX of the cathode was undertaken with the aim of best resolving a fluorine map. The relationships between the accelerating voltage and dwell time with scattering, X-ray deconvolution, and spatial resolution of fluorine were explored. The structure of the cathode consists of large NMC particles held together in a matrix by the fluorine-rich PVDF binder. The NMC particles can be seen in Figure 1a. Comparing the SE image (Figure 1a) with the fluorine map (Figure 1c) shows the fluorine map displaying a complementary shape to the NMC particles. Fewer fluorine X-rays are detected from NMC positions, and the strongest fluorine X-rays are detected where CBD is located on the SE image. Because the X-ray spectra of fluorine overlap with those of manganese and cobalt, the EDX software is challenged to deconvolute and isolate manganese and cobalt X-rays from fluorine. Figure S1 details the spectra emitted from CBD and NMC regions and shows the convolution among fluorine, manganese, and cobalt. The software has limitations and can misrepresent the fluorine signal yield emitted near NMC particles. In addition to this, the spatial resolution of fluorine can be inhibited by scattering as fluorine is highly electronegative and will deflect electrons. Sublimation of fluorine to HF is also possible,[42] contaminating SEM's vacuum environment. The consequence of both these mechanisms is demonstrated with the fluorine signal being emitted above and below the electrode in the bulk resin, which is fluorine-free, as in Figure 3a−c.

To deduce how to increase EDX's capability to spatially and spectrally resolve fluorine, three locations were imaged with different dwell times and accelerating voltages, as shown in Figure 3. The best spatially resolved fluorine map is yielded in Figure 3d, 1 scan at 5 kV for a 2500 μs dwell time. The fluorine signal is concentrated in specific locations where CBD is present and there are ellipsoidal silhouettes of fluorine signals where the NMC particles are positioned. The NMC and the

https://doi.org/10.1021/acs.jpcc.4c05678
J. Phys. Chem. C 2024, 128, 20957−20966

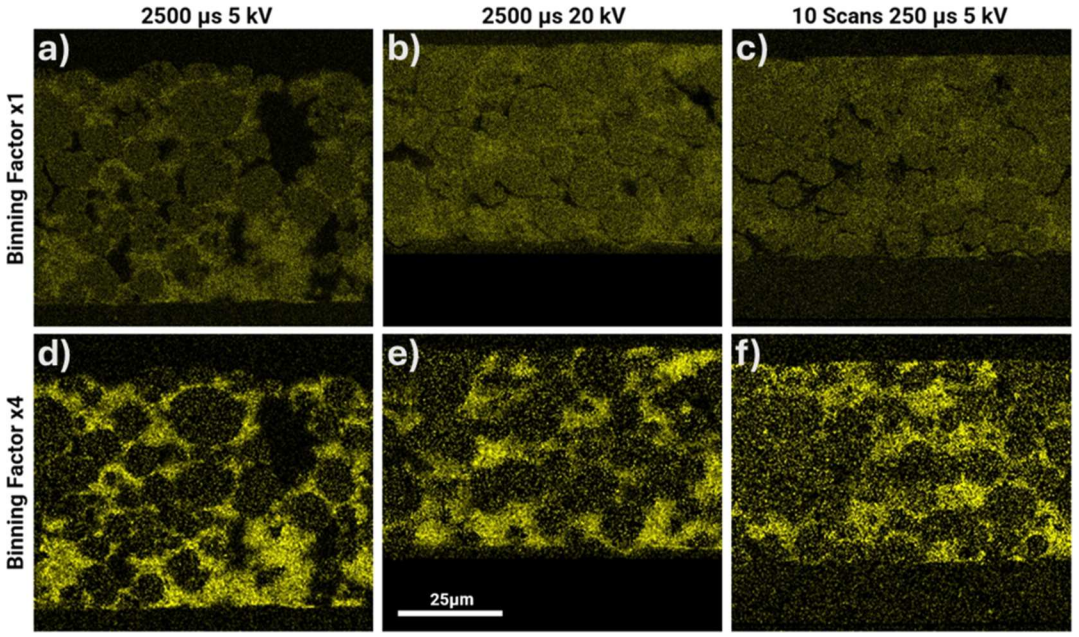

Figure 3. Fluorine maps of three electrode cross sections. All 3500× magnification, all same scale. (a) 1 scan, 2500 μs dwell time, 5 kV, (b) 1 scan, 2500 μs dwell time, 20 kV, and (c) 10 scans, 250 μs dwell time, 5 kV. Images (d–f) are images (a–c) with a binning factor of 4. The binning factor combines 4 pixels into 1, increasing the signal-to-noise ratio. The results show three integers of fluorine signals: highest signal from CBD-rich regions, moderate signal from NMC positions, and lowest signal from CBD-free resin. Scan (b) was aborted midscan, partially through the current collector.

CBD are most distinguishable in this scan. The contrast between fluorine signals is the greatest when comparing CBD-rich and CBD-free regions.

It is more challenging to differentiate between the CBD phase and NMC particles (Figure 3e and f). Inspection of Figure 3e, 1 scan at 20 kV for a 2500 μs dwell time, indicates that the higher beam energy of 20 kV creates a lower contrast between fluorine-rich zones and fluorine-free zones. It is possible to identify where NMC and the CBD exist, however, not as distinctly as in Figure 3d.

Figure 3f, 10 scans at 5 kV for a 250 μs dwell time, yields the most difficult image to differentiate. The CBD can be identified. However, the contrast in signals is the least distinct. Scattering can be seen most in this image. The primary factor identified for the lack of distinguishability in Figure 3f is fluorine mobility. Fluorine migrates when mapped over multiple scans because fluorine is susceptible to being pushed through a solid polymer sample if exposed to a migration force.[43] The negative charge of beam electrons and accumulation of charge provide this force. Each passing of the beam instigates more fluorine migration, which results in a changing fluorine signal for every scan. Previously fluorine-rich areas will produce fewer signals, and fluorine-free zones will become contaminated with fluorine and produce a weak signal. The EDX map is constructed by averaging the data measured over the multiple scans, and because the data in each scan are changing, the averaged result will not be representative of the initial sample. This analysis suggests parameters used in Figure 3a,d; a 5 kV accelerating voltage and a 2500 μs dwell time for one scan yield a more representative fluorine map of the sample.

Quantifying Fluorine Mobility. A line scan analysis was conducted to quantify the fluorine mobility and fluorine count trend over multiple scans. Three indicators of fluorine mobility have been identified: changes to the line scan profile structure, the gradient of fluorine over the CBD–resin boundary, and the ratio between the total amount of fluorine detected in the CBD region against the CBD-free resin region. In every line scan, the fluorine counts in the CBD region (<0 μm) reduce between the first to fifth scans. To complement this, the fluorine counts in the CBD-free resin region (>0 μm) increase over the scans. This demonstrates the fluorine mobility mechanism; fluorine progressively migrates from the fluorine-rich region in the CBD to the fluorine-free region in resin.

The CBD phase is amorphous and inhomogeneous. This causes the structured profiles to exhibit fluorine peaks and troughs within the CBD resin, as in Figure 4. This is especially apparent in 5 kV scans. An example of this structure change is shown in Figure 4a; the first scan has counts of 225 at −5.8 μm which decreases to 40 counts at −3.8 μm before increasing back to 150 counts at −1.8 μm, displaying a U-shaped profile. The fifth scan profile fluctuates from 100 to 50 to 100 counts at the same distances −5.8, −3.8, and −1.8 μm, respectively. This still displays the U-shape, but the extent of the structure has minimized over scans. This is a consequence of fluorine-dense regions having more fluorine which can be mobilized compared to fluorine-sparse regions, which have less fluorine to be mobilized. This causes a net shift of fluorine from the rich regions to sparse regions as the movement of fluorine from rich to sparse regions is greater. The consequence of this effect is the loss of the structured profile, shifting toward a linear profile. Further scans after the fifth would be expected to minimize this structure further.

The 3.5 μm peak in Figure 4b is assumed to be anomalous. It may be due to a cluster CBD being below the escape depth of fluorine and not visible on the SE but within the interaction volume and irradiated by the beam. In this situation, fluorine mobility would be observed and lead to migration toward the surface of the sample. Once fluorine has migrated within the escape depth, fluorine X-rays would be detected, causing an

https://doi.org/10.1021/acs.jpcc.4c05678
J. Phys. Chem. C 2024, 128, 20957−20966

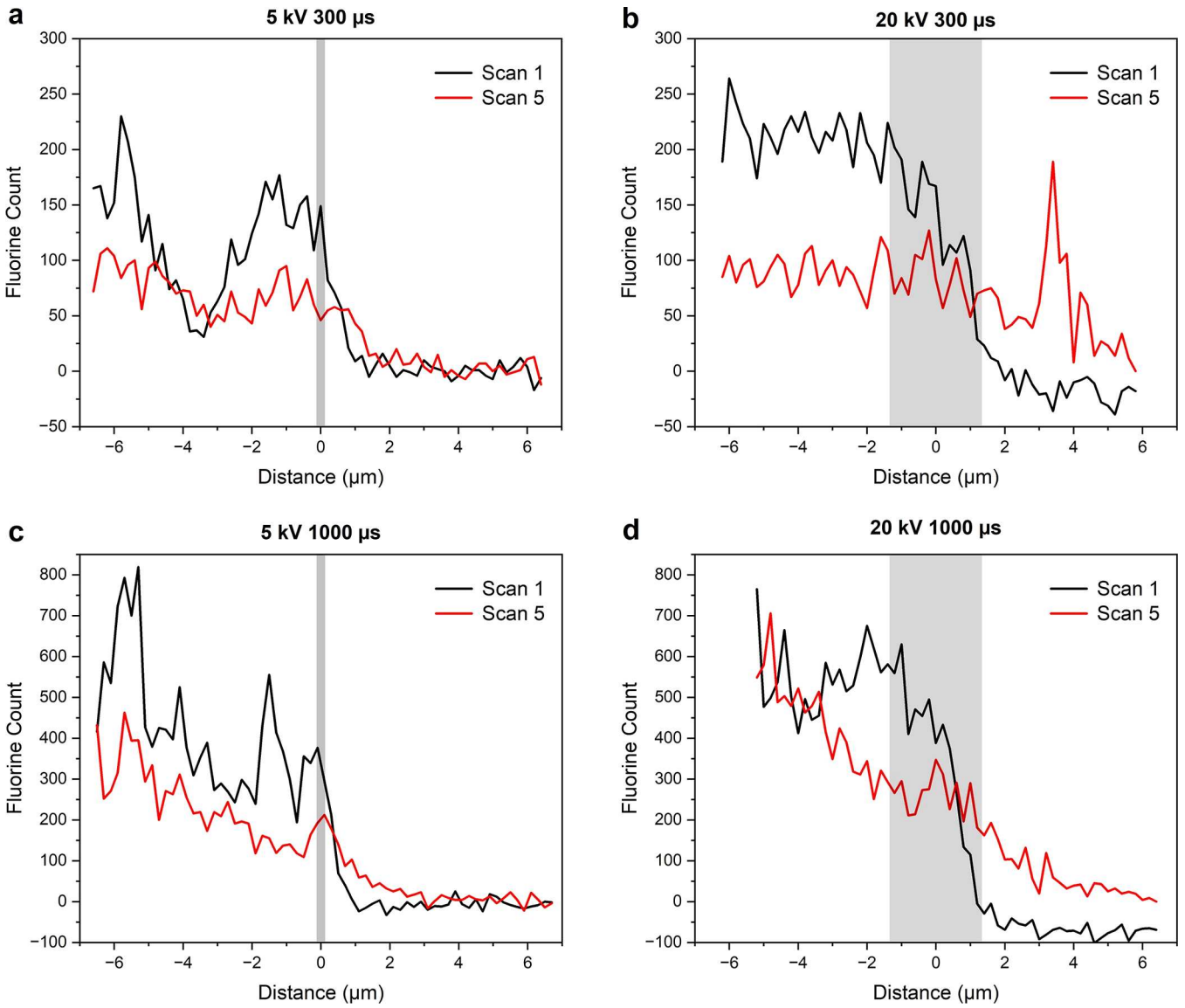

Figure 4. Fluorine line scan comparison at different accelerating voltages and dwell times. The line scan shows readings for fluorine along a 2D line which spans from CBD-rich resin to CBD-free resin, visible on the secondary electron image. 0 μm represents the CBD−resin interface and is shown as a dashed line in Figure 2. The movement of fluorine from the CBD region (<0 μm) into the resin (>0 μm) can be seen during the first to fifth scans. This is demonstrated by the counts diminishing from the first to fifth scans in the CBD region (<0 μm) and the increase in the CBD-free resin (>0 μm). Gray zones indicate the simulated interaction volumes in CASINO.

increase in fluorine content for the position. This is supported by Figure S2, which demonstrates the peak progressively increasing during the scans. Alternatively, it may be possible that the beam has damaged the resin above a CBD cluster. This could narrow the thickness of the resin to below the escape depth of the fluorine. This would lead to an increase in fluorine counts as new fluorine X-rays can reach the EDX detector.

The boundary between the CBD and the CBD-free resin is also an indicator because it measures the signal change as the beam transitions from a fluorine-rich zone to a fluorine-free zone. The boundary gradient changes for different process conditions and across scans in Figure 4a−d. The changes seen between the first and fifth scans are a decrease in the boundary gradient, an increase in the boundary distance length, and increasing fluorine counts within the first 2 μm of the CBD-free resin. This is explained by the migration of fluorine into the CBD-free resin, decreasing the distinctiveness of the boundary as fluorine infiltrates the CBD-free resin.

The difference in the boundary gradient between 5 and 20 kV is also profound. The gradient for 5 kV shown in Figure 4a,b is much steeper than 20 kV, shown in Figure 4c,d. The effect of fluorine mobility should be minimal during the initial scan; therefore, beam interaction volume will dominate the boundary gradient for the first scans. All line scan measurements were taken in 100 nm integers; therefore, the larger interaction volume of a 20 kV accelerating voltage causes the CBD region to still be measured when scanning further into the CBD-free resin. The beam interaction volumes simulated in modeling software Monte Carlo Simulation (CASINO) version 2.4.8[44] shown in Figure 5 demonstrate a 238 nm radius at a 5 kV accelerating voltage compared to a 2553 nm radius at 20 kV (considering 90% of interaction energy). 1000 electrons were simulated for both 5 and 20 kV. Simulated interaction

https://doi.org/10.1021/acs.jpcc.4c05678
J. Phys. Chem. C 2024, 128, 20957−20966

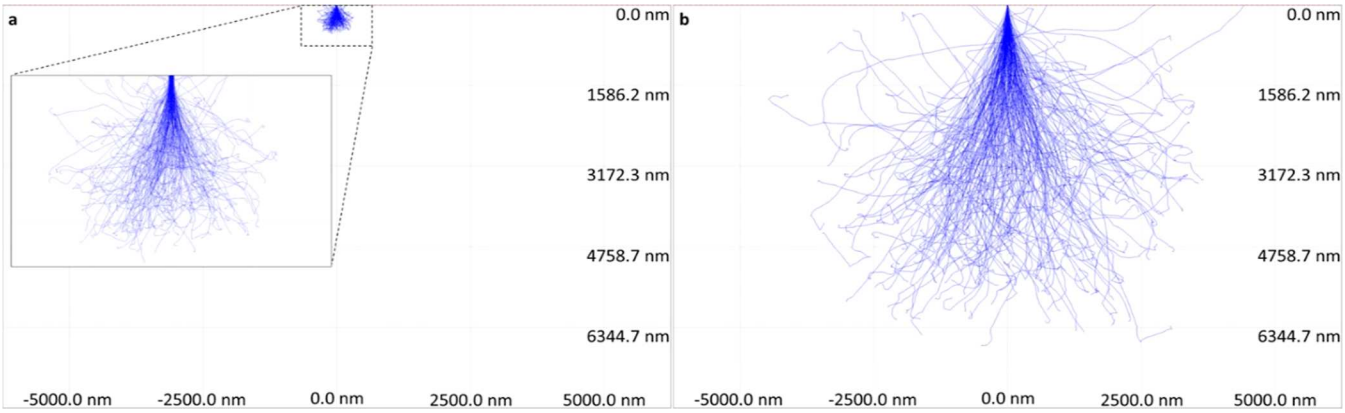

Figure 5. CASINO simulations of interaction volumes within the resin at (a) 5 and (b) 20 kV. The interaction volume shapes are similar, but their magnitudes and resin penetration are significantly different. The radius of the interaction volume correlates with spatial resolution. A better spatial resolution is to be expected for 5 kV due to the smaller interaction volume radius.

volumes have been displayed as gray zones in Figure 4, centered over the CBD resin boundary. There is a positive correlation between interaction volume and the boundary gradient. The smaller interaction volume, 5 kV, exhibits a steeper gradient. The interaction volume difference between 5 and 20 kV is significant[45] and demonstrates why the loss of spatial resolution is widely accepted for higher accelerating voltages[46] in addition to the extent of beam damage.[47] Interaction volumes simulated in this work are similar to other literature looking into EDX analysis of fluoropolymer samples.[48]

Limitations of this technique include mislabeling of the CBD−resin boundary and measuring negative fluorine counts. X-ray emissions during EDX involve much larger interaction volumes than those of backscattered or secondary electrons. This creates an opportunity to misalign the line scan data with the SE/BSE image because there may be CBD that is too deep to be detected by backscattered electrons but may be excited to emit X-rays. This should be considered when labeling the border between the CBD and the resin. Despite this, our data has aligned well and the CBD−resin gradients span similar lengths to the simulated interaction volumes for both 5 and 20 kV.

Negative fluorine counts are due to measurement errors arising from limitations of the EDX detector and EDX software. The electron beam causes continuum background X-rays; the incident electrons decelerate as they pass through the Coulombic field of the specimen and emit X-rays at all energies below the incidence beam energy.[49] This means that background X-rays are produced at characteristic wavelengths, which inflate the X-ray counts of these elements. AZtec, the EDX software, can account for this inflation and eliminate the background X-rays with "Tru-Q" an EDX quantitative algorithm.[50] The algorithm is useful and is employed during maps and scans in this report. However, due to fluorine having a weak X-ray signal, the error associated with the elimination of background X-rays is large enough to cause negative fluorine counts when fluorine is absent or in low concentration. This is especially apparent at 20 kV because the incident beam electrons have vastly more energy. The more energy each electron has, the more it can interact with the sample and lose energy during deceleration, producing more background X-rays. This advocates for the use of the 5 kV accelerating voltage because 20 kV causes a significant increase in background X-rays for a less significant increase in fluorine X-rays. To demonstrate the effect of the software, line scans with the Tru-Q algorithm disabled are demonstrated in Figure S3. It shows positive fluorine counts across all regions and increased fluorine counts for the whole line scan because the software does not compensate for background X-rays.

Sample Degradation and Complete Elemental Analysis. The X-ray signal emitted by fluorine has been documented in the literature to reduce the more the sample is imaged.[48] This is applicable to other elements as the sample incurs damage and is radiated during imaging; however, fluorine has been identified as a particularly susceptible element. Raw fluorine EDX data was extracted and analyzed, as seen in Figure 6. A common trend displayed was the total fluorine counts decreasing to approximately 70% from the first to fifth line scans. Additionally, the counts drop to around 80% after the first scan, indicating the importance of limiting the beam's interaction with fluorine. It can also be seen that dwell time has a greater influence over increasing the X-ray counts

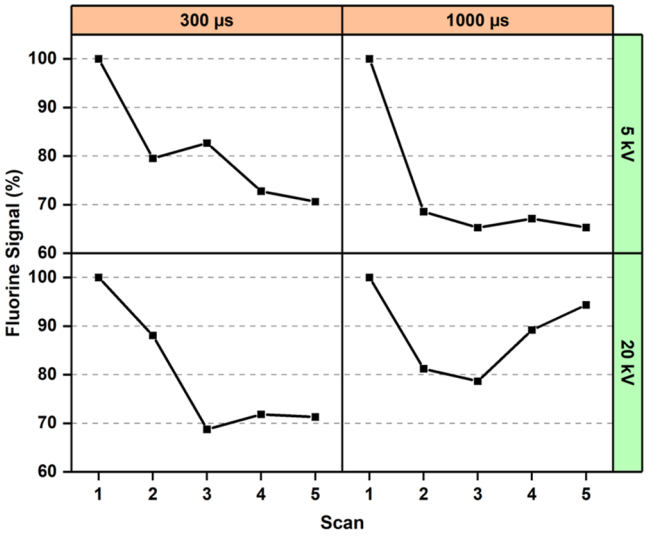

Figure 6. Fluorine signal for each scan relative to the first scan, demonstrating the loss of X-rays over the line scans. The first scan measures the highest fluorine count in all parameters, before decreasing over further scans. 300 and 1000 μs dwell times and 5 and 20 kV accelerating voltages have been compared.

https://doi.org/10.1021/acs.jpcc.4c05678
J. Phys. Chem. C 2024, 128, 20957−20966

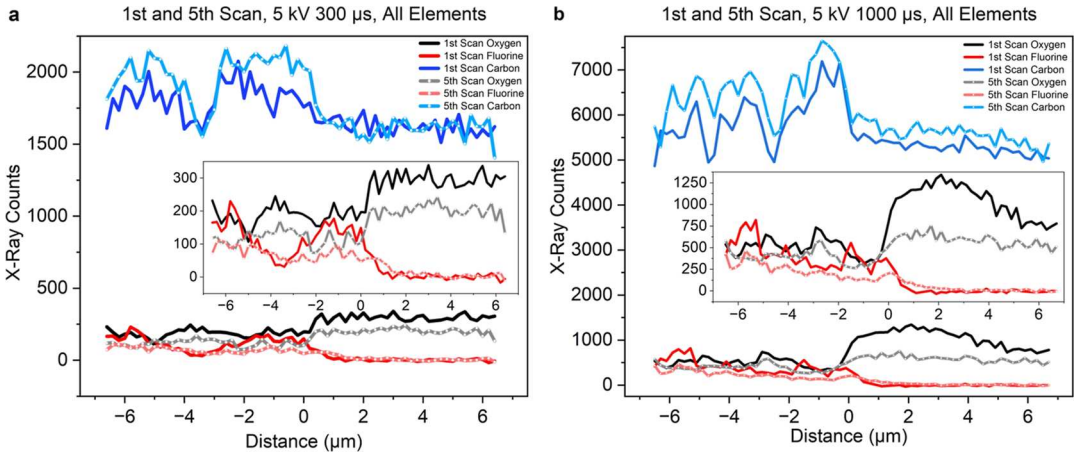

Figure 7. Line scans of the CBD boundary comparing the first and fifth scans for 350 and 1000 μs dwell times at 5 kV. The detectable elements were carbon, fluorine, and oxygen and have all been included. The difference in counts can be seen between the first and fifth scans and shows that carbon is stable but oxygen and fluorine are not. The abundance of carbon is due to the epoxy resin impregnation.

compared to dwell time. This is due to the weak fluorine X-rays having a weak escape velocity. A large fraction of the X-rays generated in the large interaction volume of 20 kV will not reach the detector. Increasing the dwell time increases the time for which the X-rays are measured and will consequently increase the quantity of X-rays measured.

To compare the behavior between fluorine and other elements, X-rays measured during line scans for all detectable elements are shown in Figure 7. This includes fluorine, oxygen, and carbon. Carbon is abundant because it makes up the bulk of the resin and is also present in the conductive additive. Oxygen is a component of the resin. Dwell times of 300 and 1000 μs at 5 kV are examined to provide insight into the difference between lower and higher energy inputs. The comparison indicates that the fluorine signal diminishes at a greater rate compared to oxygen and carbon during repeated scans for both dwell times, evidencing that fluorine counts are more prone to diminishing. Figures 6 and 7 indicate that the first scan during EDX analysis provides the most representative data for the sample before it is degraded and skewed by electron beam damage.

Additional Considerations for Industrial Application. Scanning electron microscopes and EDX detectors have progressed significantly and are available in a range of advancements.[51] EDX detectors may have a greater surface area, which can capture more X-ray counts. Detectors can be windowless or possess thinner films, meaning the minimum energy for X-ray detection is lower.[52] Windowless detectors can detect the smallest elements, including lithium.[53] This would be advantageous when imaging fluorine because fluorine's weak X-rays are susceptible to rapidly losing energy escaping the sample. These advantages would increase the count of measured X-rays. The methodology discussed in this paper would still benefit any fluorine map attained by more advanced EDX detectors; however, it may not require as much optimization to achieve an appropriate spatial resolution of fluorine.

In contrast, the electrode formulation in this paper has a 4% PVDF binder compared to industrial formulations of 2%. Fluorine X-ray counts positively correlate with fluorine content; therefore, the fluorine counts exhibited are expected to be halved with 2% PVDF content. Fluorine would demonstrate the same behavior in these electrodes but may require further optimization to reach the confidence achieved in this work. The dominant binder in dry processing is PTFE.[54] PTFE contains double the stoichiometry of fluorine compared to PVDF. This would yield double the fluorine counts, making EDX of fluorine easier to detect compared to PVDF. This indicates the potential of fluorine maps within the dry electrode industry in addition to the wet electrode industry. Another popular lithium-ion chemistry is lithium iron phosphate (LFP). Iron possesses similar Kα energy to cobalt and manganese, and therefore fluorine, and will present similar challenges in formulations where NMC has been substituted for LFP.

Electron microscopy suffers from trajectory errors when the imaging substrate is not flat which can cause artifact defects such as shadowing and curtaining.[55,56] This is particularly applicable to electrodes that are macroporous with spherical particles. X-rays released from the sides of particles are more difficult to detect, biasing the data. Charge can also accumulate at vertices of the substrate which deflect and repel incidence electrons.[57] Casting the substrate in resin forms a uniform flat surface which reduces shadowing and dissipates charge build-up if the surface is electronically conductive.[58] Dissipating the charging and the measurement of X-rays emitted from a flat surface will yield a more representative EDX analysis. The filling of pores with resin is also advantageous when imaging a cross section. Due to a narrow beam diameter, scanning electron microscopes have a greater depth of field than optical systems;[55] this can lead to incorporating signals from deep pores. This is unideal as a cross section should represent only a superficial sample. Differentiating the superficial signal from pores with resin has been proven advantageous.[51] In our samples, the resin being a denser material than the vacuum helps reduce the trajectory depth of the electrons and escape velocity of the characteristics X-rays,[49] reducing the signal measured from these pores.

CONCLUSIONS

Multiple EDX parameters were tested for the analysis of NMC cathodes. Regarding accelerating voltage, the map and line scan results suggest that using 20 kV reduces the spatial resolution of imaging fluorine in the sample. The fluorine counts between the CBD-rich resin and the CBD−resin are less distinct compared to using 5 kV. An accelerating voltage of 20 kV also

https://doi.org/10.1021/acs.jpcc.4c05678
J. Phys. Chem. C 2024, 128, 20957−20966

induces more fluorine mobility as there is more negative charge to induce the mechanism. It causes more infiltration of fluorine into previously fluorine-free regions. Scans at 20 kV also induce more background continuum X-rays, which can inflate the fluorine count or interfere with the accuracy of measuring fluorine when attempting to eliminate background X-rays.

Regarding the scan rate and dwell time, a singular scan at a high dwell time was proven to produce a higher signal contrast between CBD and CBD-free locations in the fluorine EDX maps compared to a lower dwell time for multiple scans. In concurrence with the map, line scans indicated fewer fluorine counts within the CBD during repeated scans and a gradual rise of fluorine in the resin regions. This result was concluded to be due to the mobility of fluorine. The fluorine response that best represented the CBD phase in this study was a 5 kV accelerating voltage at 2500 μs for one singular scan. To make the most representative binder maps, these parameters should be used.

■ ASSOCIATED CONTENT

Supporting Information

The Supporting Information is available free of charge at https://pubs.acs.org/doi/10.1021/acs.jpcc.4c05678.

Additional data and raw microscopy data (PDF)

■ AUTHOR INFORMATION

Corresponding Author

Denis Cumming − *Department of Chemical and Biological Engineering, University of Sheffield, Sheffield S1 3JD, U.K.;* orcid.org/0000-0003-1923-2250; Email: d.cumming@sheffield.ac.uk

Authors

James Parker − *Department of Chemical and Biological Engineering, University of Sheffield, Sheffield S1 3JD, U.K.;* orcid.org/0009-0009-4312-1949

Rachel Smith − *Department of Chemical and Biological Engineering, University of Sheffield, Sheffield S1 3JD, U.K.*

Complete contact information is available at: https://pubs.acs.org/10.1021/acs.jpcc.4c05678

Notes

The authors declare no competing financial interest.

■ ACKNOWLEDGMENTS

The authors thank the financial support provided by the project of "Nextrode" funded by the Faraday Institution, UK (Grant number: FIRG015). The authors thank the Sheffield Sorby Centre for Electron Microscopy for use of their facilities.

■ REFERENCES

(1) Schoo, A.; Moschner, R.; Hülsmann, J.; Kwade, A. Coating Defects of Lithium-Ion Battery Electrodes and Their Inline Detection and Tracking. *Batteries* **2023**, *9* (2), 111.

(2) Keppeler, M.; Roessler, S.; Braunwarth, W. Production Research as Key Factor for Successful Establishment of Battery Production on the Example of Large-Scale Automotive Cells Containing Nickel-Rich LiNi0.8Mn0.1Co0.1O2 Electrodes. *Energy Technol.* **2020**, *8* (6), 2000183.

(3) Mohanty, D.; Hockaday, E.; Li, J.; Hensley, D. K.; Daniel, C.; Wood, D. L. Effect of Electrode Manufacturing Defects on Electrochemical Performance of Lithium-Ion Batteries: Cognizance of the Battery Failure Sources. *J. Power Sources* **2016**, *312*, 70−79.

(4) Entwistle, J.; Ge, R.; Pardikar, K.; Smith, R.; Cumming, D. Carbon Binder Domain Networks and Electrical Conductivity in Lithium-Ion Battery Electrodes: A Critical Review. *Renewable Sustainable Energy Rev.* **2022**, *166*, 112624.

(5) Fransson, L.; Eriksson, T.; Edström, K.; Gustafsson, T.; Thomas, J. O. Influence of Carbon Black and Binder on Li-Ion Batteries. *J. Power Sources* **2001**, *101* (1), 1−9.

(6) Markevich, E.; Salitra, G.; Aurbach, D. Influence of the PVdF Binder on the Stability of LiCoO2 Electrodes. *Electrochem. Commun.* **2005**, *7* (12), 1298−1304.

(7) Chen, H.; Ling, M.; Hencz, L.; Ling, H. Y.; Li, G.; Lin, Z.; Liu, G.; Zhang, S. Exploring Chemical, Mechanical, and Electrical Functionalities of Binders for Advanced Energy-Storage Devices. *Chem. Rev.* **2018**, *118* (18), 8936−8982.

(8) Gaikwad, A. M.; Arias, A. C. Understanding the Effects of Electrode Formulation on the Mechanical Strength of Composite Electrodes for Flexible Batteries. *ACS Appl. Mater. Interfaces* **2017**, *9* (7), 6390−6400.

(9) Müller, M.; Schneider, L.; Bohn, N.; Binder, J. R.; Bauer, W. Effect of Nanostructured and Open-Porous Particle Morphology on Electrode Processing and Electrochemical Performance of Li-Ion Batteries. *ACS Appl. Energy Mater.* **2021**, *4* (2), 1993.

(10) Lu, X.; Bertei, A.; Finegan, D. P.; Tan, C.; Daemi, S. R.; Weaving, J. S.; O'Regan, K. B.; Heenan, T. M. M.; Hinds, G.; Kendrick, E.; Brett, D. J. L.; Shearing, P. R. 3D Microstructure Design of Lithium-Ion Battery Electrodes Assisted by X-Ray Nano-Computed Tomography and Modelling. *Nat. Commun.* **2020**, *11*, 2079.

(11) Hein, S.; Danner, T.; Westhoff, D.; Prifling, B.; Scurtu, R.; Kremer, L.; Hoffmann, A.; Hilger, A.; Osenberg, M.; Manke, I.; Wohlfahrt-Mehrens, M.; Schmidt, V.; Latz, A. Influence of Conductive Additives and Binder on the Impedance of Lithium-Ion Battery Electrodes: Effect of Morphology. *J. Electrochem. Soc.* **2020**, *167* (1), 013546.

(12) Salitra, G.; Markevich, E.; Afri, M.; Talyosef, Y.; Hartmann, P.; Kulisch, J.; Sun, Y.-K.; Aurbach, D. High-Performance Cells Containing Lithium Metal Anodes, LiNi0.6Co0.2Mn0.2O2 (NCM 622) Cathodes, and Fluoroethylene Carbonate-Based Electrolyte Solution with Practical Loading. *ACS Appl. Mater. Interfaces* **2018**, *10* (23), 19773−19782.

(13) Zahnow, J.; Bernges, T.; Wagner, A.; Bohn, N.; Binder, J. R.; Zeier, W. G.; Elm, M. T.; Janek, J. Impedance Analysis of NCM Cathode Materials: Electronic and Ionic Partial Conductivities and the Influence of Microstructure. *ACS Appl. Energy Mater.* **2021**, *4* (2), 1335−1345.

(14) Choi, S.; Feng, W.; Xia, Y. High Entropy and Co-Free High Nickel Based Layered LiNi0.9Mn0.1O2 Cathode for Li-Ion Batteries. *ACS Appl. Energy Mater.* **2024**, *7* (8), 3339−3346.

(15) She, S.; Zhou, Y.; Hong, Z.; Huang, Y.; Wu, Y. Surface Coating of NCM-811 Cathode Materials with g-C3N4 for Enhanced Electrochemical Performance. *ACS Omega* **2022**, *7* (28), 24851−24857.

(16) Nikpour, M.; Mazzeo, B. A.; Wheeler, D. R. A Model for Investigating Sources of Li-Ion Battery Electrode Heterogeneity: Part II. Active Material Size, Shape, Orientation, and Stiffness. *J. Electrochem. Soc.* **2021**, *168* (12), 120518.

(17) Font, F.; Protas, B.; Richardson, G.; Foster, J. M. Binder Migration during Drying of Lithium-Ion Battery Electrodes: Modelling and Comparison to Experiment. *J. Power Sources* **2018**, *393*, 177−185.

(18) Baunach, M.; Jaiser, S.; Schmelzle, S.; Nirschl, H.; Scharfer, P.; Schabel, W. Delamination Behavior of Lithium-Ion Battery Anodes: Influence of Drying Temperature during Electrode Processing. *Drying Technol.* **2016**, *34* (4), 462−473.

(19) Jaiser, S.; Funk, L.; Baunach, M.; Scharfer, P.; Schabel, W. Experimental Investigation into Battery Electrode Surfaces: The Distribution of Liquid at the Surface and the Emptying of Pores during Drying. *J. Colloid Interface Sci.* **2017**, *494*, 22−31.

(20) Jaiser, S.; Müller, M.; Baunach, M.; Bauer, W.; Scharfer, P.; Schabel, W. Investigation of Film Solidification and Binder Migration

during Drying of Li-Ion Battery Anodes. *J. Power Sources* **2016**, *318*, 210−219.
(21) Zhang, Y. S.; Courtier, N. E.; Zhang, Z.; Liu, K.; Bailey, J. J.; Boyce, A. M.; Richardson, G.; Shearing, P. R.; Kendrick, E.; Brett, D. J. L. A Review of Lithium-Ion Battery Electrode Drying: Mechanisms and Metrology. *Adv. Energy Mater.* **2022**, *12* (2), 2102233.
(22) Doeff, M. M.; Wilcox, J. D.; Kostecki, R.; Lau, G. Optimization of Carbon Coatings on LiFePO4. *J. Power Sources* **2006**, *163* (1), 180−184.
(23) Morasch, R.; Landesfeind, J.; Suthar, B.; Gasteiger, H. A. Detection of Binder Gradients Using Impedance Spectroscopy and Their Influence on the Tortuosity of Li-Ion Battery Graphite Electrodes. *J. Electrochem. Soc.* **2018**, *165* (14), A3459−A3467.
(24) Klemens, J.; Schneider, L.; Herbst, E. C.; Bohn, N.; Müller, M.; Bauer, W.; Scharfer, P.; Schabel, W. Drying of NCM Cathode Electrodes with Porous, Nanostructured Particles Versus Compact Solid Particles: Comparative Study of Binder Migration as a Function of Drying Conditions. *Energy Technol.* **2022**, *10* (4), 2100985.
(25) Lain, M. J.; Apachitei, G.; Román-Ramírez, L.; Copley, M.; Marco, J. Cross-Sectional Analysis of Lithium Ion Electrodes Using Spatial Autocorrelation Techniques. *Phys. Chem. Chem. Phys.* **2022**, *24* (48), 29999−30009.
(26) Dayani, S.; Markötter, H.; Schmidt, A.; Widjaja, M. P.; Bruno, G. Multi-Level X-Ray Computed Tomography (XCT) Investigations of Commercial Lithium-Ion Batteries from Cell to Particle Level. *J. Energy Storage* **2023**, *66*, 107453.
(27) Kastner, J.; Harrer, B.; Requena, G.; Brunke, O. A Comparative Study of High Resolution Cone Beam X-Ray Tomography and Synchrotron Tomography Applied to Fe- and Al-Alloys. *NDT&E Int.* **2010**, *43* (7), 599−605.
(28) Seshadri, K.; Froyd, K.; Parikh, A. N.; Allara, D. L.; Lercel, M. J.; Craighead, H. G. Electron-Beam-Induced Damage in Self-Assembled Monolayers. *J. Phys. Chem.* **1996**, *100* (39), 15900−15909.
(29) Xiao, C.; Li, Z.; Guthrey, H.; Moseley, J.; Yang, Y.; Wozny, S.; Moutinho, H.; To, B.; Berry, J. J.; Gorman, B.; Yan, Y.; Zhu, K.; Al-Jassim, M. Mechanisms of Electron-Beam-Induced Damage in Perovskite Thin Films Revealed by Cathodoluminescence Spectroscopy. *J. Phys. Chem. C* **2015**, *119* (48), 26904−26911.
(30) Pyrz, W. D.; Park, S.; Vogt, T.; Buttrey, D. J. Electron Beam-Induced Fragmentation and Dispersion of Bi−Ni Nanoparticles. *J. Phys. Chem. C* **2007**, *111* (29), 10824−10828.
(31) Pfaffmann, L.; Jaiser, S.; Müller, M.; Scharfer, P.; Schabel, W.; Bauer, W.; Scheiba, F.; Ehrenberg, H. New Method for Binder and Carbon Black Detection at Nanometer Scale in Carbon Electrodes for Lithium Ion Batteries. *J. Power Sources* **2017**, *363*, 460−469.
(32) Scipioni, R.; Jørgensen, P. S.; Ngo, D.-T.; Simonsen, S. B.; Liu, Z.; Yakal-Kremski, K. J.; Wang, H.; Hjelm, J.; Norby, P.; Barnett, S. A.; Jensen, S. H. Electron Microscopy Investigations of Changes in Morphology and Conductivity of LiFePO4/C Electrodes. *J. Power Sources* **2016**, *307*, 259−269.
(33) Goldstein, J. I.; Newbury, D. E.; Echlin, P.; Joy, D. C.; Lyman, C. E.; Lifshin, E.; Sawyer, L.; Michael, J. R. X-Ray Spectral Measurement: EDS and WDS. In *Scanning Electron Microscopy and X-ray Microanalysis*, 3rd ed.; Springer US: Boston, MA, 2003; pp 297−353..
(34) Marshall, J. E.; Zhenova, A.; Roberts, S.; Petchey, T.; Zhu, P.; Dancer, C. E. J.; McElroy, C. R.; Kendrick, E.; Goodship, V. On the Solubility and Stability of Polyvinylidene Fluoride. *Polymers* **2021**, *13* (9), 1354.
(35) Burdette-Trofimov, M. K.; Armstrong, B. L.; Korkosz, R. J.; Tyler, J. L.; McAuliffe, R. D.; Heroux, L.; Doucet, M.; Hoelzer, D. T.; Kanbargi, N.; Naskar, A. K.; Veith, G. M. Understanding the Solution Dynamics and Binding of a PVDF Binder with Silicon, Graphite, and NMC Materials and the Influence on Cycling Performance. *ACS Appl. Mater. Interfaces* **2022**, *14* (20), 23322−23331.
(36) Wang, Y.; Yang, X.; Meng, Y.; Wen, Z.; Han, R.; Hu, X.; Sun, B.; Kang, F.; Li, B.; Zhou, D.; Wang, C.; Wang, G. Fluorine Chemistry in Rechargeable Batteries: Challenges, Progress, and Perspectives. *Chem. Rev.* **2024**, *124* (6), 3494−3589.
(37) Purser, S.; Moore, P. R.; Swallow, S.; Gouverneur, V. Fluorine in Medicinal Chemistry. *Chem. Soc. Rev.* **2008**, *37* (2), 320−330.
(38) Wood, M.; Li, J.; Ruther, R. E.; Du, Z.; Self, E. C.; Meyer, H. M.; Daniel, C.; Belharouak, I.; Wood, D. L. Chemical Stability and Long-Term Cell Performance of Low-Cobalt, Ni-Rich Cathodes Prepared by Aqueous Processing for High-Energy Li-Ion Batteries. *Energy Storage Mater.* **2020**, *24*, 188−197.
(39) Seo, J. H.; Na, S.; Ahn, S. J.; Park, K.; Lee, S.; Lee, J.; Kwon, J.-H. Electron Beam-Induced Effects on a Ni-Rich Layered Cathode Material: A Comprehensive Investigation Using STEM and EELS. *J. Phys. Chem. C* **2024**, *128* (22), 9099−9104.
(40) Pacansky, J.; Waltman, R. J.; Maier, M. Irradiation of Poly(Perfluoropropylene Oxide) by a 25-kV Electron Beam: Electron Beam Induced Chemistry of Poly(Perfluoropropylene Oxide) in the Absence of Oxygen. *J. Phys. Chem.* **1987**, *91* (5), 1225−1236.
(41) Leijten, Z. J. W. A.; Keizer, A. D. A.; de With, G.; Friedrich, H. Quantitative Analysis of Electron Beam Damage in Organic Thin Films. *J. Phys. Chem. C* **2017**, *121* (19), 10552−10561.
(42) Torrisi, L.; Percolla, R. Ion Beam Processing of Polyvinylidene Fluoride. *Nucl. Instrum. Methods Phys. Res. Sect. B Beam Interact. Mater. At.* **1996**, *117* (4), 387−391.
(43) Rajendran, S.; Cribb, B. W.; Stewart, A.; Zalucki, M.; Noller, B.; Truss, R. W. The molecular arrangement of Bifenthrin® in ether based polyurethane: Designing a synthetic termite barrier. *J. Appl. Polym. Sci.* **2010**, *116* (3), 1635−1639.
(44) Drouin, D.; Couture, A.; Joly, D.; Tastet, X.; Aimez, V.; Gauvin, R. CASINO V2.42—A Fast and Easy-to-use Modeling Tool for Scanning Electron Microscopy and Microanalysis Users. *Scanning* **2007**, *29*, 92−101.
(45) Goldstein, J. I.; Newbury, D. E.; Echlin, P.; Joy, D. C.; Lyman, C. E.; Lifshin, E.; Sawyer, L.; Michael, J. R. Electron Beam−Specimen Interactions. In *Scanning Electron Microscopy and X-ray Microanalysis*, 3rd ed.; Springer US: Boston, MA, 2003; pp 61−98..
(46) Goldstein, J. I.; Newbury, D. E.; Echlin, P.; Joy, D. C.; Lyman, C. E.; Lifshin, E.; Sawyer, L.; Michael, J. R. Image Formation and Interpretation. In *Scanning Electron Microscopy and X-ray Microanalysis*, 3rd ed.; Springer US: Boston, MA, 2003; pp 99−193..
(47) Stevens, S. M.; Cubillas, P.; Jansson, K.; Terasaki, O.; Anderson, M. W. Nanoscale Electron Beam Damage Studied by Atomic Force Microscopy. *J. Phys. Chem. C* **2009**, *113* (43), 18441−18443.
(48) Vandi, L.-J.; Truss, R.; Veidt, M.; Rasch, R.; Heitzmann, M. T.; Paton, R. Fluorine Mobility During SEM-EDX Analysis: A Challenge for Characterizing Epoxy/Fluoropolymer Interfaces. *J. Phys. Chem. C* **2013**, *117* (33), 16933−16941.
(49) Goldstein, J. I.; Newbury, D. E.; Echlin, P.; Joy, D. C.; Lyman, C. E.; Lifshin, E.; Sawyer, L.; Michael, J. R. Generation of X-Rays in the SEM Specimen. In *Scanning Electron Microscopy and X-ray Microanalysis*, 3rd ed.; Springer US: Boston, MA, 2003; pp 271−296..
(50) Rowlands, N.; Burgess, S.; Goulden, J.; Hyde, A. Determining the Chemical and Microstructural Distribution of Phases in Real-Time Using Tru-Q and Tru-I Technology. *Microsc. Microanal.* **2012**, *18* (S2), 1226−1227.
(51) Streli, C.; Wobrauschek, P.; Schraik, I. Comparison of SiLi Detector and Silicon Drift Detector for the Determination of Low Z Elements in Total Reflection X-Ray Fluorescence. *Spectrochim. Acta, Part B* **2004**, *59* (8), 1211−1213.
(52) Pommé, S.; Paepen, J.; Peräjärvi, K.; Turunen, J.; Pöllänen, R. Conversion Electron Spectrometry of Pu Isotopes with a Silicon Drift Detector. *Appl. Radiat. Isot.* **2016**, *109*, 183−188.
(53) Oleshko, V.; Fastow, E.; Scott, K.; Cumings, J. Experimental Evaluation of Lithium Detection Limits by Windowless SDD EDXS and EELS in a Binary Al-Li Alloy Powder. *Microsc. Microanal.* **2020**, *26* (S2), 986−987.
(54) Sadan, M. K.; Lian, G. J.; Smith, R. M.; Cumming, D. Co, Ni-Free Ultrathick Free-Standing Dry Electrodes for Sustainable Lithium-Ion Batteries. *ACS Appl. Energy Mater.* **2023**, *6* (24), 12166−12171.

https://doi.org/10.1021/acs.jpcc.4c05678
J. Phys. Chem. C 2024, 128, 20957−20966

(55) Ersoy, O.; Aydar, E.; Gourgaud, A.; Bayhan, H. Quantitative Analysis on Volcanic Ash Surfaces: Application of Extended Depth-of-Field (Focus) Algorithm for Light and Scanning Electron Microscopy and 3D Reconstruction. *Micron* **2008**, *39* (2), 128−136.
(56) Chen, C.-L.; Thomson, R. C. The Combined Use of EBSD and EDX Analyses for the Identification of Complex Intermetallic Phases in Multicomponent Al−Si Piston Alloys. *J. Alloys Compd.* **2010**, *490* (1−2), 293−300.
(57) Shaffner, T. J.; Veld, R. D. V. Charging" Effects in the Scanning Electron Microscope. *J. Phys. [E]* **1971**, *4* (9), 633−637.
(58) Limandri, S.; Carreras, A.; Trincavelli, J. Effects of the Carbon Coating and the Surface Oxide Layer in Electron Probe Microanalysis. *Microsc. Microanal. Off. J. Microsc. Soc. Am. Microbeam Anal. Soc. Microsc. Soc. Can.* **2010**, *16*, 583−593.

https://doi.org/10.1021/acs.jpcc.4c05678
J. Phys. Chem. C 2024, 128, 20957−20966